A&A 592, A11 (2016)
DOI: 10.1051/0004-6361/201526976
© ESO 2016

The XXL Survey: First results

Astronomy & Astrophysics
Special feature

The XXL Survey[⋆,⋆⋆]

XII. Optical spectroscopy of X-ray-selected clusters and the frequency of AGN in superclusters

E. Koulouridis[1,2], B. Poggianti[3], B. Altieri[4], I. Valtchanov[4], Y. Jaffé[5], C. Adami[6], A. Elyiv[7,8], O. Melnyk[9,10], S. Fotopoulou[11], F. Gastaldello[12], C. Horellou[13], M. Pierre[1], F. Pacaud[14], M. Plionis[15,2,16], T. Sadibekova[1], and J. Surdej[17]

[1] Service d'Astrophysique AIM, DSM/IRFU/SAp, CEA Saclay, 91191 Gif-sur-Yvette, France
e-mail: `elias.koulouridis@cea.fr`
[2] Institute for Astronomy & Astrophysics, Space Applications & Remote Sensing, National Observatory of Athens, Palaia Penteli, 15236 Athens, Greece
[3] INAF–Astronomical Observatory of Padova, Vicolo Osservatorio 5, 35122 Padova, Italy
[4] European Space Astronomy Centre (ESA/ESAC), Operations Department, Villanueva de la Canãda, Madrid, Spain
[5] Department of Astronomy, Universidad de Concepción, Casilla 160-C, Concepción, Chile
[6] LAM, OAMP, Université Aix-Marseille, CNRS, Pôle de l'Étoile, Site de Château Gombert, 38 rue Frédéric Joliot-Curie, 13388 Marseille 13 Cedex, France
[7] Dipartimento di Fisica e Astronomia, Università di Bologna, viale Berti Pichat 6/2, 40127 Bologna, Italy
[8] Main Astronomical Observatory, Academy of Sciences of Ukraine, 27 Akademika Zabolotnoho St., 03680 Kyiv, Ukraine
[9] Department of Physics, University of Zagreb, Bijenicka cesta 32, 10000 Zagreb, Croatia
[10] Astronomical Observatory, Taras Shevchenko National University of Kyiv, 3 Observatorna St., 04053 Kyiv, Ukraine
[11] Department of Astronomy, University of Geneva, Chemin d'Écogia 16, 1290 Versoix, Switzerland
[12] INAF–IASF–Milano, via Bassini 15, 20133 Milano, Italy
[13] Dept. of Earth and Space Sciences, Chalmers University of Technology, Onsala Space Observatory, 439 92 Onsala, Sweden
[14] Argelander-Institut für Astronomie, University of Bonn, Auf dem Hügel 71, 53121 Bonn, Germany
[15] Physics Department of Aristotle University of Thessaloniki, University Campus, 54124 Thessaloniki, Greece
[16] Instituto Nacional de Astrofísica Optica y Electrónica, CP 72840 Puebla, México
[17] Institut d'Astrophysique et de Géophysique, Université de Liège, 4000 Liège, Belgium

Received 16 July 2015 / Accepted 26 November 2015

ABSTRACT

Context. This article belongs to the first series of XXL publications. It presents multifibre spectroscopic observations of three 0.55 deg^2 fields in the XXL Survey, which were selected on the basis of their high density of X-ray-detected clusters. The observations were obtained with the AutoFib2+WYFFOS (AF2) wide-field fibre spectrograph mounted on the 4.2 m *William Herschel* Telescope.
Aims. The paper first describes the scientific rationale, the preparation, the data reduction, and the results of the observations, and then presents a study of active galactic nuclei (AGN) within three superclusters.
Methods. To determine the redshift of galaxy clusters and AGN, we assign high priority to a) the brightest cluster galaxies (BCGs), b) the most probable cluster galaxy candidates, and c) the optical counterparts of X-ray point-like sources. We use the outcome of the observations to study the projected (2D) and the spatial (3D) overdensity of AGN in three superclusters.
Results. We obtained redshifts for 455 galaxies in total, 56 of which are counterparts of X-ray point-like sources. We were able to determine the redshift of the merging supercluster XLSSC-e, which consists of six individual clusters at $z \sim 0.43$, and we confirmed the redshift of supercluster XLSSC-d at $z \sim 0.3$. More importantly, we discovered a new supercluster, XLSSC-f, that comprises three galaxy clusters also at $z \sim 0.3$. We find a significant 2D overdensity of X-ray point-like sources only around the supercluster XLSSC-f. This result is also supported by the spatial (3D) analysis of XLSSC-f, where we find four AGN with compatible spectroscopic redshifts and possibly one more with compatible photometric redshift. In addition, we find two AGN (3D analysis) at the redshift of XLSSC-e, but no AGN in XLSSC-d. Comparing these findings with the optical galaxy overdensity we conclude that the total number of AGN in the area of the three superclusters significantly exceeds the field expectations. All of the AGN found have luminosities below 7×10^{42} erg s^{-1}.
Conclusions. The difference in the AGN frequency between the three superclusters cannot be explained by the present study because of small number statistics. Further analysis of a larger number of superclusters within the 50 deg^2 of the XXL is needed before any conclusions on the effect of the supercluster environment on AGN can be reached.

Key words. galaxies: active – galaxies: clusters: general – X-rays: galaxies: clusters – galaxies: interactions – galaxies: evolution – large-scale structure of Universe

---

[⋆] Based on observations obtained with *XMM-Newton*, an ESA science mission with instruments and contributions directly funded by ESA Member States and NASA. Based on observations obtained with the *William Herschel* telescope during semester 13B.

[⋆⋆] The Master Catalogue is available at the CDS via anonymous ftp to `cdsarc.u-strasbg.fr` (`130.79.128.5`) or via
`http://cdsarc.u-strasbg.fr/viz-bin/qcat?J/A+A/592/A2`

1. Introduction

As structures grow hierarchically, galaxies are accreted by progressively more massive dark matter halos, and the majority of galaxies end up in clusters (Eke et al. 2004; Calvi et al. 2011). Clusters are therefore the predominant environment of galaxies and can play a very important role in establishing galaxy properties.

Although there is no explicit classification, galaxy concentrations with more than 50 members and more massive than 10^{14} $M_\odot$ are defined as galaxy clusters. Less massive aggregations with less than 50 galaxies are called galaxy groups. We note that according to the above classification most of the extended X-ray sources in the current study are clusters.

Clusters and groups are usually identified by optical and infrared surveys as concentrations of red-sequence galaxies (e.g. Gladders & Yee 2000; Koester et al. 2007a; Hao et al. 2010; Rykoff et al. 2014; Bleem et al. 2015) or galaxy overdensities in photometric redshift space (e.g. Wen et al. 2009, 2012; Szabo et al. 2011) and they are confirmed by follow-up spectroscopy. They can also be identified by X-ray observations as extended sources, unambiguously testifying the presence of hot gas trapped in the potential well of a virialised system (e.g. Pierre et al. 2004; Pacaud et al. 2007; Pierre et al. 2016, hereafter Paper I). X-ray selected cluster samples are rarer and smaller than optically selected ones, and deep X-ray observations are required to probe a significant range of halo masses.

The properties of galaxy populations in groups and clusters vary enormously. At low redshift, it is well known that some galaxy groups are dominated by early-type, passively evolving galaxies, similarly to clusters, while others have a galaxy population resembling that of the field, mostly composed of late-type, star-forming galaxies (Zabludoff & Mulchaey 1998). Recent studies of optically selected clusters at intermediate redshifts have found a similar variety. Surveys like EDisCS (Poggianti et al. 2006, 2009), *z*COSMOS (Iovino et al. 2010), and CNOC2 (Wilman et al. 2005, 2008) find that cluster galaxies differ significantly from galaxies that reside in lower mass halos in the field, but with a wide range of properties at a given cluster velocity dispersion. Whether this variety originates from the difference between virialised clusters and clusters in formation or from unbound galaxy associations is still an open question, especially given the broad spread in galaxy properties observed in the currently small X-ray selected samples (Jeltema et al. 2007; Urquhart et al. 2010).

The effect of the group and cluster environment on the activity of the central supermassive black hole (SMBH) of galaxies and vice versa is still fairly undetermined, but nevertheless crucial. Galaxy clusters represent one end of the density spectrum in our universe, and as such they are an ideal place to investigate the effect of the dense environment in the triggering of active galactic nuclei (AGN), especially since an excessive number of X-ray point-like sources are undoubtedly found there (e.g. Cappi et al. 2001; Molnar et al. 2002; Johnson et al. 2003; D'Elia et al. 2004; Cappelluti 2005; Gilmour et al. 2009). Specifically, for the XMM-LSS field, 60% of X-ray-selected AGN reside in the overdense regions of group-like environment (Melnyk et al. 2013). We note that AGN can be used as cosmological probes to trace the large-scale structure at high redshifts (e.g. Einasto et al. 2014), and thus the study of the AGN frequency-to-density relation is essential.

Theoretically, the feeding of the black hole can only be achieved by means of a non-axisymmetric perturbation that induces mass inflow. This kind of perturbation can occur in interactions and merging between two galaxies, which results in the feeding of the black hole and the activation of the AGN phase (e.g. Umemura 1998; Kawakatu et al. 2006; Koulouridis et al. 2006a,b; 2013; Koulouridis 2014; Ellison et al. 2011; Silverman et al. 2011; Villforth et al. 2012; Hopkins & Quataert 2011). Thus, the cluster environment, where the concentration of galaxies is very high relative to the field, would also seem favourable to AGN. However, the rather extreme conditions within the gravitational potential of a galaxy cluster can work in the opposite direction as well. The ram pressure from the intracluster medium (ICM) is probably able to strip or evaporate the cold gas reservoir of galaxies (Gunn & Gott 1972; Cowie & Songaila 1977; Giovanelli & Haynes 1985; Chung et al. 2009; Jaffé et al. 2015) and can strongly affect the fueling of the AGN. Other studies, however, have argued that ram pressure stripping cannot be as effective in transforming blue-sequence galaxies to red (e.g. Larson et al. 1980; Balogh et al. 2000, 2002; Bekki et al. 2002; van den Bosch et al. 2008; Wetzel et al. 2012), especially in galaxy groups where other processes are taking place as well. In addition, possible prevention of accretion of gas from the halo into cluster or group galaxies ("strangulation"; e.g. Larson et al. 1980; Bekki et al. 2002; Tanaka et al. 2004) may, in fact, suppress AGN activity.

When using only optically selected AGN, the results on the AGN frequency within galaxy clusters remain inconclusive. Early studies reported that AGN are less frequent in galaxy clusters than in the field (Osterbrock 1960; Gisler 1978; Dressler et al. 1985) and more recent studies support this suggestion (Kauffmann et al. 2004; Popesso & Biviano 2006; von der Linden et al. 2010; Pimbblet et al. 2013). Other studies, however, have found no differences between cluster and field galaxies (e.g. Miller et al. 2003).

In contrast to optically selected AGN, radio-loud AGN seem to be more clustered than any other type of galaxy (Hart et al. 2009) and are often associated with brightest cluster galaxies (BCGs; e.g. Best 2004; Best et al. 2007). Nevertheless, Best et al. (2005) showed that radio-loud AGN with the strongest optical emission lines avoid the densest regions, a fact that implies a certain connection between the environment and the accretion rate onto the SMBH.

Undoubtedly, the best way to detect active galaxies is through X-ray observations (e.g. Brandt & Alexander 2010). During the previous decade, spectroscopic studies of X-ray point-like sources in rich galaxy clusters have concluded that low-X-ray-luminosity AGN ($<3 \times 10^{42}$ erg s^{-1}) are equally present in cluster and field environments (e.g. Martini et al. 2007; Haggard et al. 2010), although most of them presented no optical AGN spectrum (e.g. Martini et al. 2002, 2006; Davis et al. 2003). Nevertheless, luminous AGN were rarely found in clusters (Kauffmann et al. 2004; Popesso & Biviano 2006). More recent studies also reported a significant lack of AGN in rich galaxy clusters by comparing X-ray to optical data. Koulouridis & Plionis (2010) demonstrated the suppression of X-ray-selected AGN in 16 rich Abell clusters (Abell 1958) by comparing the X-ray point source overdensity to the optical galaxy overdensity. Ehlert et al. (2013, 2014) found that the X-ray AGN fraction in the central regions of 42 of the most massive clusters known is about three times lower than the field value using the same technique, while in their most recent study (Ehlert et al. 2015) they argue that galaxy mergers may be an important contributor to the cluster AGN population. More importantly, from the complete spectroscopy of their X-ray point-like source sample, Haines et al. (2012) concluded that X-ray

AGN found in massive clusters are an in-falling population and confirm the suppression in the inner regions of rich clusters. On the other hand, Martini et al. (2013) argue that this trend is not confirmed for a sample of high-redshift clusters ($1.0 < z < 1.5$). Finally, an indirect way to address the issue is by clustering analyses, but these results also remain inconclusive (see relevant discussion in Haines et al. 2012, Sect. 5.2).

The majority of the above studies deal with AGN within massive clusters, while the presence of AGN in less massive or even more massive formations has been very poorly studied. In a scenario in which AGN are suppressed by the strong gravitational potential of massive clusters (through gas stripping, strangulation, tidal stripping, evaporation, high velocity-dispersion, etc.), one would expect the AGN presence to rise in shallower gravitational potentials (see Arnold et al. 2009; Gavazzi et al. 2011; Bitsakis et al. 2015) and be completely nullified within the deepest ones. In Koulouridis et al. (2014), we investigated the AGN presence in two samples of poor and moderate clusters and found evidence of this anti-correlation. Interestingly, in merging or actively growing clusters the high incidence of galaxy mergers can potentially enhance the number of AGN, while at the same time, shock waves may also enhance the ram pressure stripping intensity (Vijayaraghavan & Ricker 2013; Jaffé et al., in prep.).

In the current study we investigate the most extreme massive formations in the Universe, superclusters. They typically consist of three to ten clusters spanning as many as 150 h^{-1} Mpc and are without sharply defined boundaries (e.g. Chon et al. 2014; Pearson 2015). The superclusters can vary widely in size, containing from a few small groups of the order of 10^{13}–10^{14} $M_{\odot}$ (e.g. Einasto et al. 2011; Chon et al. 2014) up to many massive clusters. We note, however, that the mass density, averaged on the supercluster scale, is smaller than in clusters. They are already decoupled from the Hubble flow, but not yet virialised; the time it takes a randomly moving galaxy to traverse the long axis of a supercluster is typically comparable to the age of the universe. They also appear to be interconnected, but the boundaries between them are poorly defined. At these large scales the dynamical evolution proceeds at a slow rate and superclusters reflect the initial conditions of their formation. Therefore, they are important sites where we can directly witness the evolution of structure formation and mass assembly.

With its depth, uniform coverage, and well-defined selection function, the XXL Survey (The Ultimate *XMM-Newton* Survey, Paper I) is making a unique contribution to the study of distant clusters. In addition, its two 5×5 deg^2 fields are essential to the study of AGN in the cluster environment. Clusters can be very extended, of the order of a few Mpc, and AGN may preferentially reside even further out in their outskirts (e.g. Fassbender et al. 2012; Haines et al. 2012; Koulouridis et al. 2014). More than half of the detected extended sources are 1−3 keV clusters in the $0.2 < z < 0.5$ range (Fig. 1), they cover an estimated mass range $10^{12.8}$–$10^{14.5}$ $M_{\odot}$, and are the subject of our spectroscopic follow-up campaign.

In the first part of the current paper (Sects. 2 and 3), we present the preparation, the data reduction, and the results of the *William Herschel* Telescope (WHT) observations. In the second part (Sect. 4) we investigate the AGN frequency within the three superclusters. The results for cluster galaxies and the related spectroscopic catalogues will be presented in a subsequent paper. Throughout this paper we use $H_0 = 70$ km s^{-1} Mpc^{-1}, $\Omega_{\rm m} = 0.28$, and $\Omega_{\Lambda} = 0.72$.

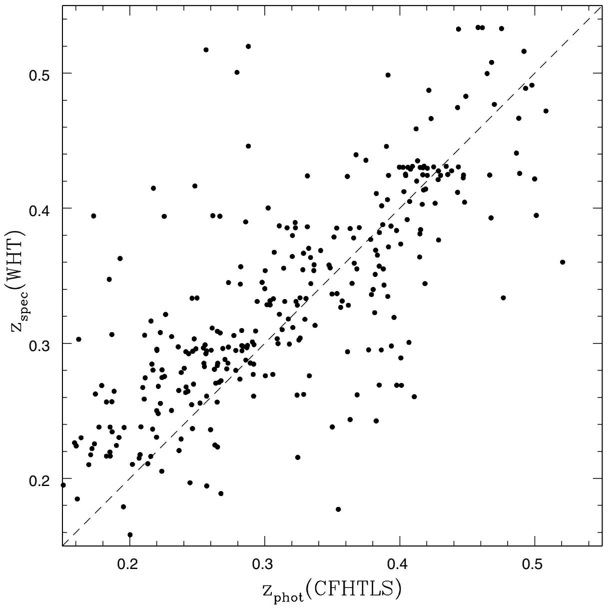

Fig. 1. Comparison of the galaxy spectroscopic redshifts obtained during the two runs with the *William Herschel* Telescope with the CFHTLS photometric redshifts.

2. Data description

2.1. The XXL Survey

The XXL Survey is the largest XMM project approved to date (>6 Ms), surveying two ~5×5 deg^2 fields at a depth of ~5×10^{-15} erg s^{-1} cm^{-2} in the [0.5−2] keV soft X-ray band[1] (completeness limit for the point-like sources). The XXL observations have been completed and processed. To date some 450 new galaxy clusters have been detected out to redshift $z \sim 2$ as well as more than 10 000 AGN out to $z \sim 4$. The main goal of the project is to constrain the Dark Energy equation of state using clusters of galaxies. This survey will also have lasting legacy value for cluster scaling laws and studies of galaxy clusters, AGN, and X-ray background. The northern field (XXL-N), which we use in the current study, is also covered in other wavelengths, e.g. the Canada-France-Hawaii Telescope Legacy Survey (CFHTLS-optical), *Spitzer* Space Telescope (SST-infrared), the UKIRT Infrared Deep Sky Survey (UKIDSS) and the Galaxy Evolution Explorer (GALEX-Ultraviolet).

2.2. Spectroscopic target and supercluster selection

The three fields observed in this work (see Table 1) were chosen on the basis of the high number of X-ray clusters, containing a total of 25 X-ray groups/clusters in the redshift range that we are targeting, i.e. $0.2 < z < 0.5$. In order of priority, we targeted a) all the BCGs, b) cluster galaxy candidates selected on the basis

---

[1] The *XXM-Newton* observation IDs used in the current study:
Field-1:
0677670135, 0677670136, 0677680101, 0677680131, 0677681101
Field-2:
0651170501, 0651170601, 0655343860, 0677650132, 0677650133, 0677650134, 0677660101, 0677660201, 0677660231, 0677660232, 0677660233, 0677670133, 0677670134, 0677670135, 0742430101
Field-3:
0109520201, 0109520301, 0111110101, 0111110201, 0111110701, 0112680101, 0112680401, 0112681001, 0112681301, 0677580131, 0677580132, 0677590131, 0677590132, 0677590133.

Table 1. WHT observations.

Date (1)	Time UT (2)	Name (3)	Config. (4)	Exp. (5)	Seeing (6)
2013 Oct. 29	22:00–00:50	Field-1	1st Bright	150	$1.5''-2.4''$
2013 Oct. 29	01:42–04:45	Field-1	2nd Bright	150	$1.5''-2.4''$
2013 Oct. 30	22:00–00:15	Field-3	1st Bright	120	$<1.5''$
2013 Oct. 30	00:50–04:30	Field-1	Faint	200	$<1.5''$
2013 Nov. 07	22:00–02:10	Field-3	Faint	240	$<1.5''$
2013 Nov. 08	21:00–00:20	Field-3	2nd Bright	180	$>1.5''$
2013 Nov. 08	01:20–02:20	Field-2	1st Bright	60	$>1.5''$
2013 Nov. 09	23:00–02:30	Field-2	2nd Bright	180	$>2.0''$
2013 Nov. 10	22:00–23:30	Field-2	1st Bright	120	$>1.5''$
2013 Nov. 08	00:00–03:30	Field-2	Faint	180	$0.5''-0.9''$

Notes. (1) Date of observation; (2) starting and ending UT; (3) name of the observed WHT field; (4) target selection: "Bright" for targets $19 < m_r < 20.5$ and "Faint" for $20.5 < m_r < 21$; (5) exposure time in minutes; (6) seeing during the observation.

of projected distance to the cluster X-ray position ($<500\ h^{-1}$ kpc and $19 < r_{\rm SDSS} < 21$), c) optical counterparts of X-ray point-like sources (mostly AGN), and finally d) any other galaxy in the targeted redshift range according to their photometric redshift.

Superclusters are defined as concentrations of clusters that trace a second-order clustering hierarchy of galaxies, and they are the largest structures observed. In the current study we identify superclusters as concentrations of at least three clusters at a close redshift separation within 25′ radius, given the limited field of view (FoV) of the WHT. Our three observed fields include a total of three superclusters (see Table 2).

Pacaud et al. (2016, hereafter Paper II) base their selection on a different methodology because of the different sample (the 100 brightest clusters, hereafter XXL-100-GC[2]) and the different area (the full XXL Survey). According to Paper II a supercluster must include a close pair of clusters ($D < 8\ h^{-1}$ Mpc) and at least a third cluster within 20 h^{-1} Mpc of the pair. The above selection requires all three clusters of the starting triplet to be members of the XXL-100-GC. Then all clusters within 35 h^{-1} Mpc, independent of brightness, are considered supercluster members. They finally report five superclusters, XLSSC-a to -e.

Two of them are in common with the current paper, i.e. Field-1 includes XLSSC-e and Field-2 a part of XLSSC-d. The latter comprises seven X-ray detected clusters in Paper II, but the WHT FoV includes only a close bright pair and one more fainter cluster[3]. In Field-3 we discover a supercluster that satisfies the first criterion of Paper II of having a close pair of clusters that belong to the XXL-100-GC sample, but the third member is fainter. We name this supercluster XLSSC-f.

In addition to the discovery of the XLSSC-f supercluster, we also publish a new XXL cluster, namely XLSSC 117. We list some basic properties of the new cluster in Table 2.

3. Multifibre optical spectroscopy

3.1. Target preparation

For the preparation of the observations we executed the software `af2-configure`, available in the *Isaac Newton* Group of Telescopes (ING) website[4]. It is designed to create the mapping between the objects and the fibres during a particular spectrograph exposure. It uses an input file with the coordinates (α, δ) of the objects, creates a fibre-to-object mapping using one of two currently available placement algorithms, and then allows the user to edit the fibre locations interactively. In the input file the user should also assign priority to all objects. High priority should be assigned to fiducial stars, since it is essential to allocate approximately eight fiducial fibres, scattered homogeneously in the field, to accurately align the science fibres. The placement algorithms search for the best combination of position angle of the spectrograph on the sky and targets in the fibres that maximise the sum of object priorities.

The fibres are positioned by `af2-configure` within a FoV of 1 deg in diameter, but we manually limited our targets within the central 25 arcmin radius to avoid the effects of vignetting. We tried to maximise the number of fibres allocated on galaxies, but typically also placed 20−30 fibres on the sky for sky subtraction purposes. Within each field our targets were divided into bright ($19 < r_{\rm SDSS} < 20.5$) and faint ($20.5 < r_{\rm SDSS} < 21$) and we prepared two fibre configurations for the bright sources and one for the faint. We allocated an average of ∼100 sources per configuration, plus sky fibres and fiducial stars.

3.2. Observations

We observed the three fields with the 4.2 m WHT during six nights in 2013. More details about the observations are listed in Table 1. We conducted multifibre medium resolution spectroscopy with the AutoFib2+WYFFOS (AF2) wide-field multifibre spectrograph. The AF2 contains 150 science fibres of 1.6 arcsec diameter and 10 fiducial bundles for acquisition and guiding. At the prime focus, the fibres are placed onto a field plate by a robot positioner at user-defined sky coordinates (see Sect. 3.1).

We used the R600B grating with the new default detector Red+4. It is an e2v 231-84 4k × 4k, red-sensitive, fringe-suppression CCD with a mosaic of 4096 × 4112 pixels, 15 μm each. We used a 2 × 2 binning of the CCD pixels and we obtained a spectral resolution of ∼4.4 Å. The spectra were centred at wavelength ∼5400 Å, and covered the range 3800 to 7000 Å. The spectra of He and Ne lamps were used for the wavelength calibration.

The bright configurations were observed for 2 or 2.5 h each (depending on the seeing), and the faint for 3−4 h each. We were able to observe nine fibre configurations. In total the run yielded ∼900 spectra.

3.3. Data reduction

Data were reduced using the AF2 data reduction pipeline v1.02[5]. The pipeline is written in IDL and is able to perform data reduction, including fibre-to-fibre sensitivity corrections and optimal extraction of the individual spectra. Below we describe briefly

---

[2] XXL-100-GC data are available in computer readable form via the XXL Master Catalogue browser http://cosmosdb.iasf-milano.inaf.it/XXL, and via the XMM XXL DataBase http://xmm-lss.in2p3.fr

[3] Because of the slightly higher average redshift of the three clusters of XLSSC-d in the current paper ($z = 0.298$) than of the seven clusters in Paper II ($z = 0.294$), the two papers report slightly different redshift (0.30 and 0.29, respectively).

[4] http://www.ing.iac.es

[5] A newer version of the pipeline (v3.0) can be downloaded from http://www.ing.iac.es/astronomy/instruments/af2/reduction.html

Table 2. Superclusters.

Obs. Field (1)	RA (2)	Dec (3)	Supercluster (4)	RA (5)	Dec (6)	cluster ID (7)	$z_{\rm spec}$ (8)	$z_{\rm mean}$ (9)	$T_{\rm 300kpc}$ (10)	$M_{\rm 500,MT}$ (11)	$r_{\rm 500,MT}$ (12)	Ref. (13)
Field-1	32.60	–6.30	XLSSC-e	32.87	–6.20	XLSSC 081	0.432	0.429	$1.7^{+0.3}_{-0.2}$	0.7	0.55	5
						XLSSC 082†	0.427		$3.9^{+1.7}_{-0.6}$	2.9	0.88	5
						XLSSC 083†	0.430		$4.8^{+1.2}_{-0.9}$	4.1	0.99	4
						XLSSC 084†	0.430		$4.5^{+2.3}_{-1.5}$	3.7	0.96	4
						XLSSC 085†	0.428		$4.8^{+2.0}_{-1.0}$	4.1	0.99	4
						XLSSC 086†	0.424		$2.6^{+1.2}_{-0.6}$	1.5	0.70	5
Field-2	36.93	–4.70	XLSSC-d	37.22	–5.05	XLSSC 013	0.307	0.298	$1.6^{+0.3}_{-0.1}$	0.7	0.57	1
						XLSSC 022	0.293		$2.1^{+0.1}_{-0.1}$	1.1	0.68	2
						XLSSC 027	0.295		$2.7^{+0.4}_{-0.3}$	1.7	0.77	3
Field-3	33.12	–5.82	XLSSC-f	33.12	–5.82	**XLSSC 098**	0.297	0.298	$2.9^{+1.0}_{-0.6}$	1.9	0.81	4
						XLSSC 111	0.299		$4.5^{+0.6}_{-0.5}$	4.0	1.02	4
						XLSSC 117	0.298		$3.3^{+0.8}_{-0.7}$	2.4	0.86	6

Notes. (1) Observed field name; (2), (3) field coordinates in the J2000 system; (4) supercluster name; (5); (6), supercluster coordinates in the J2000 system, as published in Paper II for XLSSC-d and -e; (7) original cluster name in the XXL database, members of the XXL-100-GC sample in bold; (8) spectroscopic redshift; (9) mean supercluster redshift; (10) X-ray temperature in keV within an aperture of 300 kpc measured in Giles at al. (2016, Paper III) for the members of the XXL-100-GC sample; (11) cluster mass in 10^{14} $M_{\odot}$, calculated from the $M_{\rm 500,MT} - T_{\rm 300\ kpc}$ scaling relation of Lieu et al. (2016, hereafter Paper IV); (12) overdensity radius with respect to the critical density in Mpc, calculated from the $M_{\rm 500,MT} - T_{\rm 300\ kpc}$ scaling relation of Paper IV; (13) reference to the first X-ray detection as a cluster. $^{(\dagger)}$ The spectroscopic redshift of the cluster was initially determined by the observations presented in the current paper.

References. (1) Willis et al. (2005); (2) Pierre et al. (2006); (3) Pacaud et al. (2007); (4) Paper II; (5) Paper VII; (6) this work.

the calibration and extraction modules of the pipeline, but more details can be found in the pipeline manual distributed online by the ING.

The first steps of the pipeline include master bias correction, tracing of the fibres, flat-field correction, masking of bad pixel in the science data, and wavelength calibration. In more detail:

1. `BIAS` module: at least ten bias files are used each night to debias all raw data images. The average signal level in the overscan regions is used to correct for any change in the bias level over time.
2. `MASK` module: the module produces a mask file of the CCD pixels where the dark current exceeds a user-specified level. It also displays a plot of the fraction of masked pixels versus the cut-off level and an image of the produced file.
3. `FLAT` module: at least ten twilight sky or internal flats were used to perform the flat-field correction each night. Individual flats are scaled according to their mean value before calculating their total median value.
4. `CIRC` module: this module uses a flat file to trace the x-pixel position of the centre of the spectral line of each active fibre as a function of y-pixel. In the pipeline version used for the reduction in the current paper, the module crashed if the low-signal area of the CCD (the blue part of the spectrum) was not trimmed. The new version of the pipeline, however, does not present this problem and the user can analyse the CCD in its full length.
5. `ARC` & `ATLAS` module: the module extracts the lamp spectrum as a function of y-pixel position and uses this intermediate spectrum to determine the wavelength calibration. In our case two arc files are used to reference lines simultaneously, one from the helium lamp for the blue part of the spectrum, and one from the neon lamp for the red part of the spectrum. The `ARC` module identifies the approximate y-pixel location and exact wavelengths for a set of well-separated unsaturated lines in the arc spectra and finds the precise position of the peaks by fitting Gaussian profiles to each one. It uses a predefined table of emission line data, but in combination with the `ATLAS` module the selection and confirmation of the lamp lines is performed interactively.

The extraction of the spectrum by the pipeline is done in two additional steps:

1. `STAR` module: the module first extracts the science spectra of designated targets and sky-allocated fibres and then processes the intermediate spectra to produce sky subtracted output spectra on a common wavelength base. The median sky spectrum is calculated within the `STAR` module. There are four different options for the calculation, but in our case we selected the one where the median sky is scaled and the output spectrum is masked over sky lines.
2. `MEDAN` module: this module evaluates the median spectra for each fibre by combining all available science exposures. Spectra are normalised to their mean value before the median is calculated.

Finally, the flux calibration, which is not included in the pipeline, is performed with IRAF using `STANDARD`, `SENSFUNC`, and `CALIBRATE` tasks. Given the wide magnitude range covered, the spectra have a wide range of S/N.

3.3.1. Galaxy redshifts

Redshifts were obtained from visual inspection of all spectra by two of the authors (BP and CA), using the IRAF package RVSAO independently and iterating on doubtful cases.

The overall success rate (number of redshifts/number of spectra) was 60%, ranging from 84% for the best seeing configurations to the lowest 30% for the worst ones.

The probability that each redshift was correct was estimated on the basis of the number and quality of spectral features (lines in emission or absorption, D4000) identified in the spectrum. If a large number of lines were identified without wavelength offsets the probability was set to 99%. As the number of identified spectral features decreased, the assigned probability decreased; 75% percent redshifts had at least two or three secure lines.

In total we obtained 455 good-quality redshifts (of which 172/147/110 have a 75%/95%/99% chance of being correct, and 26 are based on a single emission line but with very reliable identification). Ninety other redshifts were more uncertain and were not used for any of our purposes, but were recorded for future reference. We note that our target sample was not contaminated by stars.

In more detail we obtained:

1. 9 BCG (brightest cluster galaxy) redshifts. These provide us with nine new cluster redshifts around $z = 0.3$–0.5. More importantly these redshifts are too high to be obtained by GAMA spectroscopy (Driver et al. 2011; Liske et al. 2015), which covers the XXL Survey, but is much shallower.
2. 82 and 160 cluster galaxy candidates that lie within 0.5 and 1 h^{-1} Mpc of the cluster centres, respectively. We will use these galaxies for a more precise determination of the cluster redshifts and for the study of the cluster properties.
   In addition, we obtained the redshifts of another 148 galaxies that lie more than 1 h^{-1} Mpc from the closest extended X-ray source.
3. 56 AGN redshifts that are used in the second part of the current paper, in combination with spectroscopic results from other surveys.

In Fig. 1 we compare our spectroscopic redshifts with the CFHTLS photometric redshifts (Ilbert et al. 2006; Coupon et al. 2009). WHT spectroscopy is clearly useful in the redshift range of interest ($0.2 < z < 0.5$).

4. AGN in superclusters

In the following sections we present a study of the AGN frequency in the three observed supercusters. The supercluster in Field-1 (XLSSC-e) is very different from the ones found in the other two fields, i.e. all five clusters found at $z \sim 0.43$ are located within a circle of 4′ radius (1.3 h^{-1} Mpc) and a sixth but uncertain member within 10′. A more detailed analysis of the supercluster and its BCGs is presented in Pompei et al. (2016, hereafter Paper VII). Baran et al. (2016, hereafter Paper IX) identified several overdensities via a Voronoi Tessellation analysis of optically detected galaxies and presented new radio observations. Therefore, we consider the supercluster in Field-1 to be a merging supercluster in a tight configuration.

On the contrary, in the FoV of the WHT (6.5 h^{-1} Mpc radius at $z = 0.3$), the other two structures include only three members each in a much looser configuration, although both include a very close cluster pair (<1 h^{-1} Mpc). Therefore, the superclusters in Field-2 (XLSSC-d) and Field-3 (XLSSC-f) seem very similar (see Fig. 2). However, further investigation outside the WHT FoV reveals that these two superclusters are intrinsically different, i.e. the structure found in Field-2 is only part of a larger formation comprising seven X-ray detected clusters within 35 h^{-1} Mpc (Paper II), while the three clusters found in Field-3 are not related to any significant overdensity in the region. Nevertheless, the total mass of the latter is larger by a factor of 2.5.

Because of the above differences and its higher redshift, we studied AGN in XLSSC-e within a 10′ radius around its five confirmed clusters, while for the other two superclusters we used the full 25′ FoV of the WHT. In general, superclusters are not virialised and there is no explicit definition of their centre. For XLSSC-e we chose a position approximately in the middle of the formation to be the centre, while for XLSSC-d and -f we used the centre of the WHT FoV. From the X-ray images in Fig. 2 (right panels) it is apparent that the above choices are reasonable.

4.1. Methodology

We assessed the enhancement or the suppression of AGN presence within the three superclusters by analysing both the 3D (spatial) and the 2D (projected) overdensity of X-ray point sources. We chose to analyse the 2D case as well since we lacked complete spectroscopy for all the X-ray point sources. However, we had to take into account that the 2D case is hampered by a variety of systematic effects, related for example to flux-boosting due to lensing (see discussion in Koulouridis et al. 2014). For the statistical evaluation of our results we used the confidence limits for small numbers of events in astrophysical data, based on Poisson statistics (Gehrels 1986).

To assess the 2D and 3D overdensity of AGN in the three superclusters we adopted a common lower luminosity limit for the X-ray point-like sources. We find that for the two superclusters at $z = 0.3$ a luminosity limit of $L_{(0.5-2\,\mathrm{keV})} = 2.7 \times 10^{42}$ erg s^{-1}, which corresponds to $f_{(0.5-2\,\mathrm{keV})} \sim 1.0 \times 10^{-14}$ erg s^{-1} cm^{-2}, combines both the inclusion of low-luminosity AGN and a relatively high completeness of spectroscopic redshifts. For the supercluster XLSSC-e at $z = 0.43$, this luminosity limit corresponds to a flux limit of $f_{(0.5-2\,\mathrm{keV})} = 4.5 \times 10^{-15}$ erg s^{-1} cm^{-2}. We will show the importance of having a common luminosity rather than a flux limit for fields at different redshifts.

4.1.1. Projected overdensity of X-ray point-like sources

In a given area, the projected overdensity of X-ray AGN is estimated according to

$$\delta_x = \frac{N_x}{N_{\mathrm{exp}}} - 1, \qquad (1)$$

where N_x is the number of X-ray point-like sources detected in the area and N_{exp} is the expected number according to the $\log N - \log S$ of the XXL northern field (Elyiv et al. in prep) within the same area. We note that the soft-band $\log N - \log S$ used in the current study is lower than those of the 2XMM (Ebrero et al. 2009) and COSMOS (Cappelluti et al. 2009) surveys (with deviations not exceeding the 2–3σ Poisson level), but in excellent agreement with those of the XMM Medium Deep Survey (XMDS, Chiappetti et al. 2005).

To calculate the value of N_x, we identified all point-like sources located within five radial annuli between n and $(n + 1)r$ around the centre of each field, where $n = 0, 1, 2, \ldots 5$, $r = 2'$ for XLSSC-e (higher redshift and more compact) and $r = 5'$ for XLSSC-d and XLSSC-f. The large contiguous area of the XXL Survey allowed us to expand our search for X-ray AGN at large radii.

To calculate the expected number N_{exp} of X-ray sources in the field, we followed the procedure described below, considering each time the same area of the detector and the same characteristics of the actual observation:

1. From the $\log N - \log S$ we derived the total number (N_f) of expected sources in the area per flux bin.

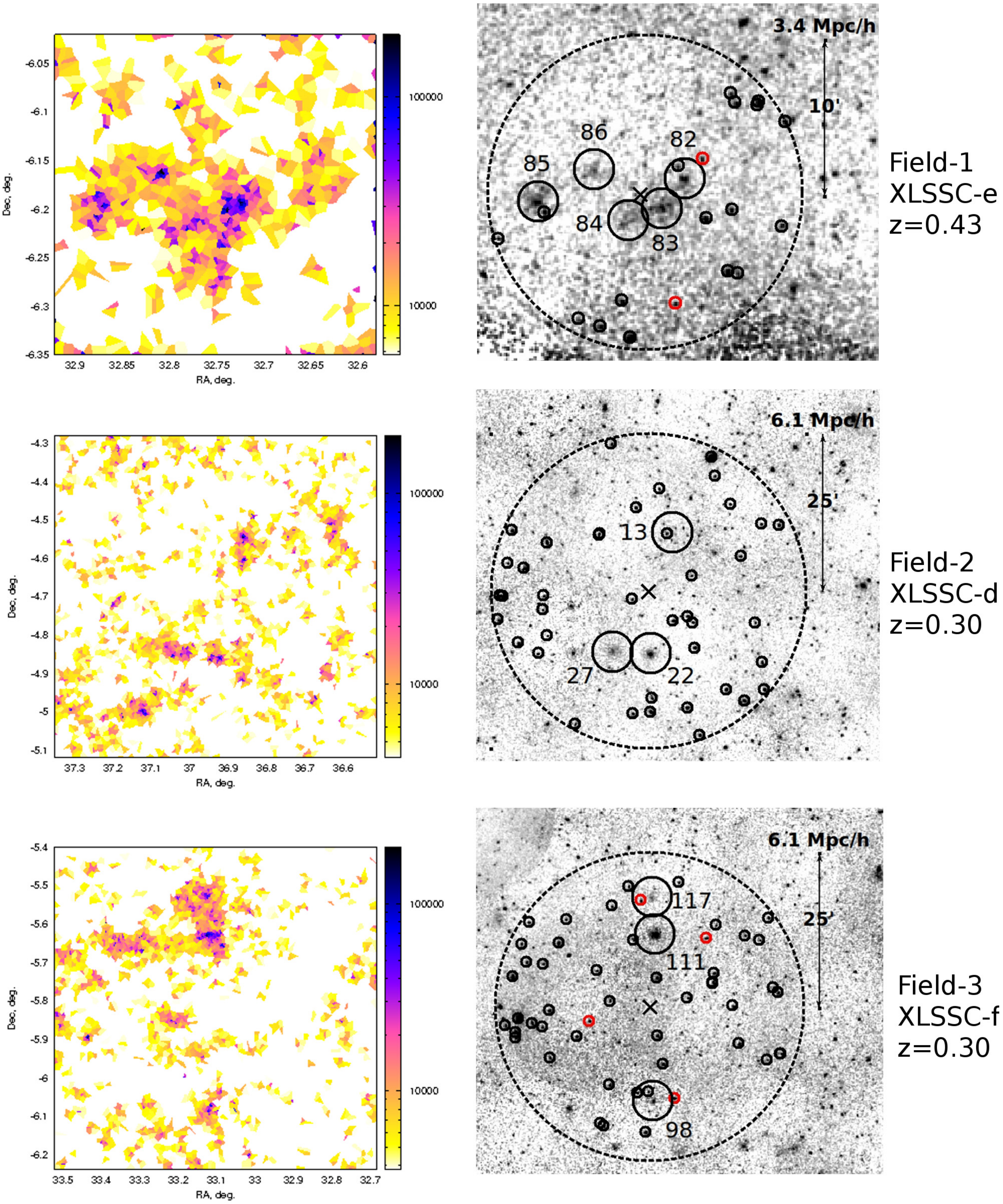

Fig. 2. Voronoi tessellations (VT) and X-ray images of the three superclusters (XLSSC-e: *top*, XLSSC-d: *middle*, XLSSC-f: *bottom*). *Left panels*: Voronoi tessellation using CFHTLS photometric redshift data. All galaxies within $\delta z = \pm 0.05$ of the supercluster redshift are included. The side bar illustrates the colour-coding of the galaxy number-density. Only areas above the average number-density are coloured in the plots. *Right panels*: the corresponding X-ray maps overplotted with the positions of the studied areas (dashed circles) and of the X-ray detected clusters (large black circles with XLSSC ID numbers). The small black circles denote X-ray point-like sources above the luminosity limit ($L_{(0.5-2\ \mathrm{keV})} > 2.7 \times 10^{42}$ erg s^{-1}), while the red circles denote the ones with spectroscopic redshift consistent with the supercluster (within $2\times\delta z$, see Sect. 4.1.2). The supercluster centres are marked with an X. The scale of the VT plots and their corresponding X-ray images is the same. The X-ray clusters can be easily identified in the high-density areas of the Voronoi plots. In the VT plots of XLSSC-d and XLSSC-f at least one more non-X-ray-detected overdensity can be seen, probably below the detection limit of the XXL Survey.

2. We considered $1000 \times N_{\rm f}$ sources with random fluxes within the flux range of each bin and random positions within the area of interest.
3. We derived the probability P_i that the source $N_{\rm fi}$ is actually detected in the specific area of the detector. The probability is a function of the off-axis position (vignetting), background, and exposure time (Elyiv et al. 2012).
4. We calculated the sum $\sum_{j=n}^{\rm nbin} \sum_{i=1}^{1000N_{\rm f}} N_{\rm fi} \times P_i/1000$, which gives the total number, $N_{\rm exp}$, of expected X-ray sources that have fluxes above the respective value of the nth bin of the $\log N - \log S$, where the total number of bins, nbin, is 160.

4.1.2. Spatial overdensity of X-ray point-like sources

Most optical counterparts of relatively bright X-ray sources ($f_{(0.5-2\ {\rm keV})} > 1.0 \times 10^{-14}$ erg s^{-1} cm^{-2}) in our three superclusters have spectroscopic redshifts. In more detail, in XLSSC-e five out of six sources have spectroscopy within a 10′ radius of the centre of the supercluster. Similarly, within the 25′ of XLSSC-d and -f we find 38 out of 41, and 38 out of 51, respectively. On the contrary, only 4 out of the 13 sources below this flux have spectroscopy in XLSSC-e (we note that in XLSSC-e the flux limit is $f_{(0.5-2\ {\rm keV})} = 4.5 \times 10^{-15}$ erg s^{-1} cm^{-2}, see Sect. 4.1).

The results of the current analysis are based mainly on spectroscopic data, although the photometric redshifts of all sources were available. The optical counterparts of the sources with no available spectra are either too faint or totally absent and are therefore improbable supercluster members. In fact, studying their redshift probability distributions (PDZ), only one source in Field-3 is possibly at the redshift of the supercluster. Photometric redshifts were calculated for all our sources with suitable AGN and quasar templates (Fotopoulou et al., in prep.).

In the case of the non-virialised superclusters the boundaries and the geometry cannot be easily defined and the clusters that form the superclusters have a spread in redshift space. Therefore, we initially based our selection of supercluster members on the condition $\delta z = |z_{\rm spec} - z_{\rm mean}| < 2000(1 + z_{\rm cl})$ km s^{-1}, where $z_{\rm spec}$ is the galaxy redshift and $z_{\rm mean}$ is the mean redshift of the supercluster members, which is a good approximation of more sophisticated cluster membership selection algorithms (e.g. Old et al. 2014 and references therein). Then, we extended the search for AGN to $1.5 \times \delta z$ and $2 \times \delta z$.

The expected spatial X-ray point-like density is calculated from the luminosity function of Hasinger et al. (2005). To this end we first calculated the volume that is defined by the limits described in the previous paragraph. This is actually a cylinder of volume V given by $V = \pi R^2 \times h$, where R is the projected radius and h is the height of the cylinder that corresponds to the distance between the lower and upper redshift[6]. Then, we integrated the luminosity function within the luminosity range of interest to calculate the expected number of sources per Mpc^3. Finally, by multiplying the two values we found the expected number of sources in the area of the superclusters. In all cases the expected number of X-ray point-like sources was less than one.

The results of the projected and the spatial X-ray overdensity analysis are summarised in Table 3.

Table 3. 2D and 3D analysis.

		2D	3D		
Name	R	N	$\pm\delta z$	$\pm 1.5 \times \delta z$	$\pm 2 \times \delta z$
(1)	(2)	(3)	(4)	(5)	(6)
XLSSC-e	10	19 (22)	2 (<1)	2 (<1)	2 (<1)
XLSSC-d	25	41 (41)	0 (<1)	0 (<1)	0 (<1)
XLSSC-f	25	51 (42)	2 (<1)	3 (<1)	4 (<1)

Notes. (1) Supercluster name; (2) projected search radius in arcmin; (3) number of detected X-ray point-like sources (in parentheses the expected number of sources calculated by the $\log N - \log S$); (4)–(6) number of AGN found within 1×, 1.5×, and $2 \times \delta z$ of the supercluster redshift $z_{\rm s}$, where $\delta z = \pm 2000(1 + z_{\rm s})$ km s^{-1} (in parentheses the expected number of sources in the respective area calculated by the luminosity function).

4.1.3. Optical galaxy spatial overdensity

Any excess of X-ray point-like sources in the area of galaxy clusters can be due to the obvious abundance of galaxies with respect to the field (see Koulouridis & Plionis 2010). Therefore, to reach a meaningful interpretation of the X-ray point source overdensity analysis, and to reach a conclusion on the enhancement or suppression of AGN, we needed first to study the optical galaxy overdensity profile in the three fields. To this end, we used the photometric redshifts of the CFHTLS-T0007 W1 field (Ilbert et al. 2006; Coupon et al. 2009) computed from three to five optical bands. The accuracy is 0.031 at $i < 21.5$ and reaches $\sigma_{\delta z/(1+z_{sp})} \sim 0.066$ at $22.5 < i < 23.5$. The fraction of outliers increases from ∼2% at $i < 21.5$ to ∼10–16% at $22.5 < i < 23.5$.

The relevant expression of the optical galaxy overdensity is similar to that of the X-ray overdensity in Eq. (1), i.e.

$$\delta_{\rm o} = \frac{N_{\rm o}}{N_{\rm o,exp}} - 1, \tag{2}$$

where $N_{\rm o}$ is the number of optical sources found in the area and $N_{\rm o,exp}$ the expected background number within the same area. For the calculation of the galaxy density, we considered the regions previously defined for the X-ray analysis. The expected galaxy density was calculated from a 2 deg^2 field within the XMM-LSS area, free from clusters in the redshift range of the superclusters.

4.2. Results

From the 2D analysis of the 10′ of XLSSC-e we expect ∼22 point-like sources above the lower flux limit, $f_{(0.5-2\ {\rm keV})} = 4.5 \times 10^{-15}$ erg s^{-1} cm^{-2}, and we actually find 19. These numbers are consistent within the 1σ confidence level (Gehrels 1986). In XLSSC-d and -e, ∼41 and ∼42 X-ray point-like sources are expected above $f_{(0.5-2\ {\rm keV})} = 1 \times 10^{-14}$ erg s^{-1} cm^{-2}, respectively. Indeed, 41 X-ray point-like sources are found in XLSSC-d. Nevertheless, in XLSSC-f we discover 51 and therefore a significant X-ray overdensity is found in the area, not consistent with the expected value at the 1σ confidence level.

Considering the available photometric and spectroscopic data (3D analysis within $\pm 2 \times \delta z$, see Table 3) we find in total six AGN with compatible spectroscopic redshifts in the area of the three superclusters (for the individual analysis see the next three paragraphs). The corresponding expected number of AGN calculated from the luminosity function (Hasinger et al. 2005) is

---

[6] The height h used in the above calculations is based on the selected δz and is larger than R so that the effect of galaxy peculiar velocities on the observed redshift distance between two sources is included.

~1.5 (~0.5 AGN per field) and therefore we calculate a total spatial AGN overdensity, $\delta_{\rm x} = 3$. As we have already pointed out, before reaching any definite conclusion we also had to consider the high density of optical galaxies in the area of superclusters. Therefore, we also assessed the total spatial overdensity of optical galaxies in the three fields, $\delta_{\rm o} = 0.42$. We conclude that there is indeed a significantly higher overdensity of AGN with respect to the corresponding overdensity of optical galaxies at the 95% confidence level (Gehrels 1986). This could indicate extra triggering of AGN caused by the environment. We note that the above result is not affected by the selection of a different redshift range ($\pm\delta z$ or $\pm 1.5\times\delta z$, see Table 3); although we detect fewer AGN, we also consider a much smaller volume.

Next, we proceed with the 3D analysis of each supercluster individually. We find two AGN at the redshift of the XLSSC-e (Field-1) within 10′ radius (Fig. 2, top). Both are low-luminosity AGN with $L_{(0.5-2\ {\rm keV})} \sim 4 \times 10^{42}$ erg s^{-1}. The detailed overdensity of optical galaxies, divided into five annuli in each field, is plotted in Fig. 3. It is apparent that in the area of XLSSC-e the bulk of the galaxies are concentrated in the central 4′, while in the last annulus the galaxy density reaches the field level. The AGN overdensity in the whole field is significantly higher than the optical galaxy overdensity at the 90% confidence level despite the small number statistics (Gehrels 1986). We also note that for the XLSSC-e, radio observations were obtained in Paper IX, but no large radio galaxies were found within the overdensities. They only associated eight radio sources with potential supercluster member galaxies; however, they are not associated with any of our X-ray point-like sources.

Similarly, in XLSSC-f (Field-3) we find two to four spectroscopically confirmed AGN compatible with the supercluster redshift (depending on the redshift range, see Sect. 4.1.2 and Table 3) and another possible member with compatible photometric redshift (Fig. 2, bottom). The optical galaxy overdensity profile (Fig. 3) is almost flat over the whole field. This is probably due to cluster XLSSC 111, which is very massive with a large $r_{500,{\rm MT}}$ radius and affects the full field. The X-ray overdensity is significantly higher than the optical overdensity at the 99% confidence level. Similar to the two AGN found in XLSSC-e, the four AGN found in XLSSC-f are low-luminosity sources ($L_{(0.5-2\ {\rm keV})} < 7 \times 10^{42}$ erg s^{-1}). The list of AGN can be found in Table 4.

In contrast, no AGN is found within a 25′ radius in XLSSC-d (Fig. 2, middle). In this field the large number of optical galaxies are located in annuli 2 to 4 (Fig. 3), as expected from the location of the three clusters, while in the first and last annuli the density reaches the expected field value. The overdensity of AGN in Field-2 is $\delta_{\rm x} = -1$, but the null hypothesis that it is consistent with the optical galaxy overdensity cannot be rejected at any statistically significant level.

We note that a low-luminosity source is actually detectable in a smaller fraction of XLSSC-e compared to the other two superclusters because of their different redshift (~15% smaller effective area for a source with $f_{(0.5-2\ {\rm keV})} \sim 5 \times 10^{-15}$ erg s^{-1} cm^{-2}). In addition, the spectroscopic completeness in XLSSC-e is less than 50%, while in XLSSC-d and -f it is 93% and 75%, respectively. Therefore, there is some probability that we have missed supercluster members in XLSSC-e, although, as we have already discussed, the photometric redshift PDZs and the images of the optical counterparts render this probability small. Only in XLSSC-f is the probability of one extra AGN high, but in this supercluster the X-ray overdensity is already high without including the non-spectroscopic sources.

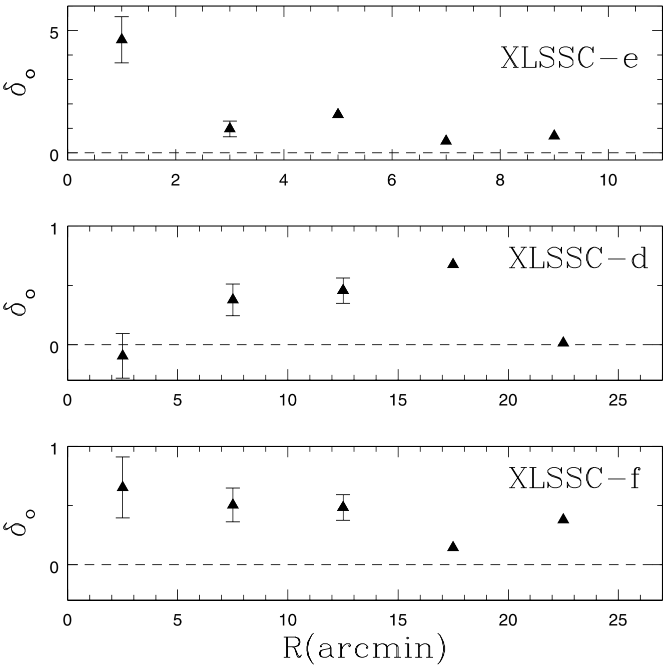

Fig. 3. Spatial overdensity profile of optical galaxies within annuli of 2′ (XLSSC-e) and 5′ (XLSSC-d, XLSSC-f) centred at the geometrical centre of the superclusters. For the calculation of the overdensity, CFHTLS photometric redshifts of galaxies were used. The error-bars are 1σ Poissonian uncertainties and are shown only for the first two or three annuli of each field. For the others the errors are smaller than the height of the symbols.

Table 4. AGN in superclusters.

Name (1)	RA (2)	Dec (3)	z (4)	$L_{(0.5-2\ {\rm keV})}$ (5)
3XLSS J021046.2-060854	32.6928	–6.1485	0.428	4.15×10^{42}
3XLSS J021053.0-061809	32.7211	–6.3026	0.423	3.66×10^{42}
3XLSS J021309.2-055142	33.2886	–5.8618	0.298	6.03×10^{42}
3XLSS J021153.5-053810†	32.9729	–5.6363	0.288	3.58×10^{42}
3XLSS J021213.7-060408†	33.0571	–6.0690	0.283	6.21×10^{42}
3XLSS J021235.9-053210	33.1499	–5.5364	0.299	6.70×10^{42}

Notes. (1) X-ray source name; (2), (3) field coordinates in the J2000 system; (4) redshift; (5) Soft X-ray luminosity in units of erg s^{-1}. $^{(\dagger)}$ Included in the 1000 brightest XXL X-ray point source catalog (Fotopoulou et al. 2016, Paper VI).

The results imply some intrinsic differences between the superclusters. XLSSC-e includes five merging clusters in tight configuration, while the three clusters of XLSSC-f are not part of any further significant overdensity. Nevertheless, their total mass is a factor of 2.5 larger than that of the three clusters of XLSSC-d. On the other hand, although the three clusters of XLSSC-d form the less massive structure, they are part of a larger overdensity that includes at least another four clusters that we have not probed with the current observations. Therefore, we cannot conclude in the current paper on the reasons that produce the observed differences because of the small number of superclusters studied. We will extend our study to the full XXL Survey in order to understand these differences better and to quantify any trend regarding the AGN frequency in the environment of superclusters.

5. Conclusions

In the first part of the current paper we presented the multifibre spectroscopic observations in three 0.55 deg^2 fields in the XXL-N survey with the 4.2 m WHT. Our targets were candidate member galaxies of clusters and optical counterparts of X-ray point-like sources. We obtained spectra for 455 galaxies, 56 of which are AGN. We determined the redshift of 25 clusters, 6 of which belong to the merging supercluster XLSSC-e at $z \sim 0.43$, and confirmed 2 more superclusters in looser configurations at $z \sim 0.3$.

In the second part, we investigated the AGN frequency in the environment of the superclusters. To this end, we identified all possible AGN supercluster members, which we define as sources with $L_{(0.5-2\ \mathrm{keV})} > 2.7 \times 10^{42}$ erg s^{-1}, and compared their projected and spatial overdensity with the expected overdensity of optical galaxies in the region. In more detail:

- XLSSC-d: the supercluster presents no significant 2D overdensity of X-ray point-like sources and the total lack of AGN found by the 3D analysis is statistically consistent with the expected number of AGN within the area.
- XLSSC-f: in sharp contrast to XLSSC-d, a high projected overdensity of X-ray point-like sources was found by the 2D analysis. This result was confirmed by the 3D analysis, where the high number of spectroscopically confirmed AGN significantly exceeded the optical galaxy density expectations.
- XLSSC-e: similarly to XLSSC-f, we find a relatively high number of spectroscopically confirmed AGN that again exceed the optical galaxy density expectations. The statistical significance of this result is not as high as for XLSSC-f and it is not supported by the 2D analysis. However, the probability that we have missed some AGN in this field is higher than in the other two fields.

Overall, the number of AGN in the area of the three superclusters significantly exceeds the field expectations at the 95% confidence level.

All six AGN found in the area of the superclusters have X-ray luminosities below 7×10^{42} erg s^{-1} and we can argue that they are low-luminosity sources. Similarly, a high number of low-luminosity AGN was reported in studies of AGN in rich clusters (e.g. Martini et al. 2002, 2006; Davis et al. 2003), but not above the field expectations (e.g. Martini et al. 2007; Haggard et al. 2010). In addition to our own data, optical spectroscopy by the SDSS-BOSS project (Dawson et al. 2013) also exists for these sources. Except for 3XLSS J021235.9-053210, none of the AGN spectra presents broad permitted emission lines. A more thorough investigation of the AGN population in superclusters will be presented in a future paper.

The reason for the difference between the AGN frequency in the three superclusters cannot be completely understood by the present study because of the small sample. To better understand the relation between AGN and the environment of superclusters, we will need to apply the same analysis to a larger number of massive formations. The wide area of the XXL Survey will soon give us the opportunity to realise this kind of study.

Acknowledgements. We would like to thank the anonymous referee for the useful comments and suggestions. XXL is an international project based around an XMM Very Large Programme surveying two 25 deg^2 extragalactic fields at a depth of 5×10^{-15} erg s^{-1} cm^{-2} in [0.5–2] keV at the 90% completeness level (see Paper I). The XXL website is `http://irfu.cea.fr/xxl`. Multiband information and spectroscopic follow-up of the X-ray sources are obtained through a number of survey programmes, summarised at `http://xxlmultiwave.pbworks.com/`. The authors acknowledge L. Chiappetti for producing a format and catalog compliance report. EK acknowledges fellowship funding provided by the Greek General Secretariat of Research and Technology in the framework of the programme Support of Postdoctoral Researchers, PE-1145. E.K. acknowledges the Centre National d'Études Spatiales (CNES) and CNRS for support of post-doctoral research. Y.J. and the Marie Curie Actions of the European Commission (FP7-COFUND) acknowledges support by FONDECYT grant N. 3130476. O.M. is grateful for the financial support provided by the NEWFELPRO fellowship project in Croatia. F.P. acknowledges support from the BMBF/DLR grant 50 OR 1117, the DFG grant RE 1462-6 and the DFG Transregio Programme TR33. This work is based on observations obtained with MegaPrime/MegaCam, a joint project of CFHT and CEA/IRFU, at the Canada-France-Hawaii Telescope (CFHT) which is operated by the National Research Council (NRC) of Canada, the Institut National des Sciences de l'Univers of the Centre National de la Recherche Scientifique (CNRS) of France, and the University of Hawaii. This work is based in part on data products produced at Terapix available at the Canadian Astronomy Data Centre as part of the Canada-France-Hawaii Telescope Legacy Survey, a collaborative project of NRC and CNRS.

References

Abell, G. O. 1958, ApJS, 3, 211
Arnold, T. J., Martini, P., Mulchaey, J. S., Berti, A., & Jeltema, T. E. 2009, ApJ, 707, 1691
Balogh, M. L., Navarro, J. F., & Morris, S. L. 2000, ApJ, 540, 113
Balogh, M., Bower, R. G., Smail, I., et al. 2002, MNRAS, 337, 256
Baran, N., Smolcic, V., Milakovic, D., et al. 2016, A&A, 592, A8 (XXL Survey, IX)
Bekki, K., Couch, W. J., & Shioya, Y. 2002, ApJ, 577, 651
Best, P. N. 2004, MNRAS, 351, 70
Best, P. N., Kauffmann, G., Heckman, T. M., et al. 2005, MNRAS, 362, 25
Best, P. N., von der Linden, A., Kauffmann, G., Heckman, T. M., & Kaiser, C. R. 2007, MNRAS, 379, 894
Bitsakis, T., Dultzin, D., Ciesla, L., et al. 2015, MNRAS, 450, 3114
Bleem, L. E., Stalder, B., Brodwin, M., et al. 2015, ApJS, 216, 20
Brandt, W. N., & Alexander, D. M. 2010, Proc. National Academy of Science, 107, 7184
Calvi, R., Poggianti, B. M., & Vulcani, B. 2011, MNRAS, 416, 727
Cappelluti, N., Cappi, M., Dadina, M., et al. 2005, A&A, 430, 39
Cappelluti, N., Brusa, M., Hasinger, G., et al. 2009, A&A, 497, 635
Cappi, M., Mazzotta, P., Elvis, M., et al. 2001, ApJ, 548, 624
Chiappetti, L., Tajer, M., Trinchieri, G., et al. 2005, A&A, 439, 413
Chon, G., Böhringer, H., Collins, C. A., & Krause, M. 2014, A&A, 567, A144
Chung, A., van Gorkom, J. H., Kenney, J. D. P, Crowl, H., & Volmer, B. 2009, AJ, 138, 1741
Coupon, J., Ilbert, O., Kilbinger, M., et al. 2009, A&A, 500, 981
Cowie, L. L., & Songaila, A. 1977, Nature, 266, 501
D'Elia, V., Fiore, F., Elvis, M., et al. 2004, A&A, 422, 11
Davis, D. S., Miller, N. A., & Mushotzky, R. F. 2003, ApJ, 597, 202
Dawson, K. S., Schlegel, D. J., Ahn, C. P., et al. 2013, AJ, 145, 10
Dressler, A., Thompson, I. B., & Shectman, S. A. 1985, ApJ, 288, 481
Driver, S. P., Hill, D. T., Kelvin, L. S., et al. 2011, MNRAS, 413, 971
Ebrero, J., Mateos, S., Stewart, G. C., Carrera, F. J., & Watson, M. G. 2009, A&A, 500, 749
Ehlert, S., Allen, S. W., Brandt, W. N., et al. 2013, MNRAS, 428, 3509
Ehlert, S., von der Linden, A., Allen, S. W., et al. 2014, MNRAS, 437, 1942
Ehlert, S., Allen, S. W., Brandt, W. N., et al. 2015, MNRAS, 446, 2709
Einasto, M., Liivamägi, L. J., Tago, E., et al. 2011, A&A, 532, A5
Einasto, M., Tago, E., Lietzen, H., et al. 2014, A&A, 568, A46
Eke, V. R., Frenk, C. S., Baugh, C. M., et al. 2004, MNRAS, 355, 769
Ellison, S. L., Patton, D. R., Mendel, J. T., & Scudder, J. M. 2011, MNRAS, 418, 2043
Elyiv, A., Clerc, N., Plionis, M., et al. 2012, A&A, 537, A131
Fassbender, R., Šuhada, R., & Nastasi, A. 2012, Adv. Astron., 2012, 138380
Fotopoulou, S., Pacaud, F., Paltani, S., et al. 2016, A&A, 592, A5 (XXL Survey, VI)
Gavazzi, G., Savorgnan, G., & Fumagalli, M. 2011, A&A, 534, A31
Gehrels, N. 1986, ApJ, 303, 336
Gilmour, R., Best, P., & Almaini, O. 2009, MNRAS, 392, 1509
Giles, P. A., Maughan, B. J., Pacaud, F., et al. 2016, A&A, 592, A3 (XXL Survey, III)
Giovanelli, R., & Haynes, M. P. 1985, ApJ, 292, 404
Gisler, G. R. 1978, MNRAS, 183, 633
Gladders, M. D., & Yee, H. K. C. 2000, AJ, 120, 2148
Gunn, J. E., & Gott, J. R., III 1972, ApJ, 176, 1
Haggard, D., Green, P. J., Anderson, S. F., et al. 2010, ApJ, 723, 1447

Haines, C. P., Pereira, M. J., Sanderson, A. J. R., et al. 2012, ApJ, 754, 97

Hao, J., McKay, T. A., Koester, B. P., et al. 2010, ApJS, 191, 254

Hart, Q. N., Stocke, J. T., & Hallman, E. J. 2009, ApJ, 705, 854

Hasinger, G., Miyaji, T., & Schmidt, M. 2005, A&A, 441, 417

Hopkins, P. F., & Quataert, E. 2011, MNRAS, 415, 1027

Ilbert, O., Arnouts, S., McCracken, H. J., et al. 2006, A&A, 457, 841

Iovino, A., Cucciati, O., Scodeggio, M., et al. 2010, A&A, 509, A40

Jaffé, Y. L., Smith, R., Candlish, G. N., et al. 2015, MNRAS, 448,1715

Jeltema, T. E., Mulchaey, J. S., Lubin, L. M., & Fassnacht, C. D. 2007, ApJ, 658, 865

Johnson, O., Best, P. N., & Almaini, O. 2003, MNRAS, 343, 924

Kauffmann, G., White, S. D. M., Heckman, T. M., et al. 2004, MNRAS, 353, 713

Kawakatu, N., Anabuki, N., Nagao, T., Umemura, M., & Nakagawa, T. 2006, ApJ, 637, 104

Koester, B. P., McKay, T. A., Annis, J., et al. 2007, ApJ, 660, 221

Koulouridis, E. 2014, A&A, 570, A72

Koulouridis, E., & Plionis, M. 2010, ApJ, 714, L181

Koulouridis, E., Plionis, M., Chavushyan, V., et al. 2006a, ApJ, 639, 37

Koulouridis, E., Chavushyan, V., Plionis, M., Krongold, Y., & Dultzin-Hacyan, D. 2006b, ApJ, 651, 93

Koulouridis, E., Plionis, M., Chavushyan, V., et al. 2013, A&A, 552, A135

Koulouridis, E., Plionis, M., Melnyk, O., et al. 2014, A&A, 567, A83

Larson, R. B., Tinsley, B. M., & Caldwell, C. N. 1980, ApJ, 237, 692

Lieu, M., Smith, G. P., Giles, P. A., et al. 2016, A&A, 592, A4 (XXL Survey, IV)

Liske, J., Baldry, I. K., Driver, S. P., et al. 2015, MNRAS, 452, 2087

Martini, P., Kelson, D. D., Mulchaey, J. S., & Trager, S. C. 2002, ApJ, 576, L109

Martini, P., Kelson, D. D., Kim, E., Mulchaey, J. S., & Athey, A. A. 2006, ApJ, 644, 116

Martini, P., Mulchaey, J. S., & Kelson, D. D. 2007, ApJ, 664, 761

Martini, P., Miller, E. D., Brodwin, M., et al. 2013, ApJ, 768, 1

Melnyk, O., Plionis, M., Elyiv, A., et al. 2013, A&A, 557, A81

Miller, C. J., Nichol, R. C., Gómez, P. L., Hopkins, A. M., & Bernardi, M. 2003, ApJ, 597, 142

Molnar, S. M., Hughes, J. P., Donahue, M., & Joy, M. 2002, ApJ, 573, L91

Old, L., Skibba, R. A., Pearce, F. R., et al. 2014, MNRAS, 441, 1513

Osterbrock, D. E. 1960, ApJ, 132, 325

Pacaud, F., Pierre, M., Adami, C., et al. 2007, MNRAS, 382, 1289

Pacaud, F., Clerc, N., Giles, P. A., et al. 2016, A&A, 592, A2 (XXL Survey, II)

Pearson, D. W. 2015, MNRAS, 449, 3212

Pierre, M., Valtchanov, I., Altieri, B., et al. 2004, J. Cosmol. Astropart. Phys., 9, 011

Pierre, M., Pacaud, F., Duc, P.-A., et al. 2006, MNRAS, 372, 591

Pierre, M., Pacaud, F., Adami, C., et al. 2016, A&A, 592, A1 (XXL Survey, I)

Pimbblet, K. A., Shabala, S. S., Haines, C. P., Fraser-McKelvie, A., & Floyd, D. J. E. 2013, MNRAS, 429, 1827

Poggianti, B. M., von der Linden, A., De Lucia, G., et al. 2006, ApJ, 642, 188

Poggianti, B. M., Aragón-Salamanca, A., Zaritsky, D., et al. 2009, ApJ, 693, 112

Pompei, E., Adami, C., Eckert, D., et al. 2016, A&A, 592, A6 (XXL Survey, VII)

Popesso, P., & Biviano, A. 2006, A&A, 460, L23

Rykoff, E. S., Rozo, E., Busha, M. T., et al. 2014, ApJ, 785, 104

Silverman, J. D., Kampczyk, P., Jahnke, K., et al. 2011, ApJ, 743, 2

Szabo, T., Pierpaoli, E., Dong, F., Pipino, A., & Gunn, J. 2011, ApJ, 736, 21

Tanaka, M., Goto, T., Okamura, S., Shimasaku, K., & Brinkmann, J. 2004, AJ, 128, 2677

Umemura, M., Fukue, J., & Mineshige, S. 1998, MNRAS, 299, 1123

Urquhart, S. A., Willis, J. P., Hoekstra, H., & Pierre, M. 2010, MNRAS, 406, 368

van den Bosch, F. C., Aquino, D., Yang, X., et al. 2008, MNRAS, 387, 79

Vijayaraghavan R., & Ricker, P. M. 2013, MNRAS, 435, 2713

Villforth, C., Sarajedini, V., & Koekemoer, A. 2012, MNRAS, 426, 360

von der Linden, A., Wild, V., Kauffmann, G., White, S. D. M., & Weinmann, S. 2010, MNRAS, 404, 1231

Wen, Z. L., Han, J. L., & Liu, F. S. 2009, ApJS, 183, 197

Wen, Z. L., Han, J. L., & Liu, F. S. 2012, ApJS, 199, 34

Wetzel, A. R., Tinker, J. L., & Conroy, C. 2012, MNRAS, 424, 232

Willis, J. P., Pacaud, F., Valtchanov, I., et al. 2005, MNRAS, 363, 675

Wilman, D. J., Balogh, M. L., Bower, R. G., et al. 2005, MNRAS, 358, 88

Wilman, D. J., Pierini, D., Tyler, K., et al. 2008, ApJ, 680, 1009

Zabludoff, A. I., & Mulchaey, J. S. 1998, ApJ, 496, 39